ACSNANO

www.acsnano.org

ARTICLE

Magnetic-Actuated Jumping of Droplets on Superhydrophobic Grooved Surfaces: A Versatile Strategy for Three-Dimensional Droplet Transportation

Yusheng Huang, Guifeng Wen, Yue Fan, Maomao He, Wen Sun, Xuelin Tian, and Shilin Huang*

Cite This: *ACS Nano* 2024, 18, 6359–6372

Read Online

ACCESS | Metrics & More | Article Recommendations | Supporting Information

ABSTRACT: On-demand droplet transportation is of great significance for numerous applications. Although various strategies have been developed for droplet transportation, out-of-surface three-dimensional (3D) transportation of droplets remains challenging. Here, a versatile droplet transportation strategy based on magnetic-actuated jumping (MAJ) of droplets on superhydrophobic grooved surfaces (SHGSs) is presented, which enables 3D, remote, and precise manipulation of droplets even in enclosed narrow spaces. To trigger MAJ, an electromagnetic field is utilized to deform the droplet on the SHGS with the aid of an attached magnetic particle, thereby the droplet acquires excess surface energy. When the electromagnetic field is quickly removed, the excess surface energy is partly converted into kinetic energy, allowing the droplet to jump atop the surface. Through high-speed imaging and numerical simulation, the working mechanism and size matching effect of MAJ are unveiled. It is found that the MAJ behavior can only be observed if the sizes of the droplets and the superhydrophobic grooves are matched, otherwise unwanted entrapment or pinch-off effects would lead to failure of MAJ. A regime diagram which serves as a guideline to design SHGSs for MAJ is proposed. The droplet transportation capacities of MAJ, including in-surface and out-of-surface directional transportation, climbing stairs, and crossing obstacles, are also demonstrated. With the ability to remotely manipulate droplets in enclosed narrow spaces without using any mechanical moving parts, MAJ can be used to design miniaturized fluidic platforms, which exhibit great potential for applications in bioassays, microfluidics, droplet-based switches, and microreactions.

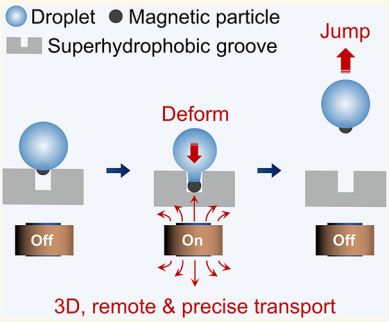

KEYWORDS: *droplet transportation, superhydrophobic surfaces, three-dimensional manipulation, magnetic particles, microfluidics*

The transportation of liquid droplets has attracted great attention due to its essential role in numerous applications, including water harvesting,[1−4] heat management,[5,6] microfluidics,[7,8] liquid separation,[9,10] *etc.* Various passive and active strategies have been developed for droplet transportation. The passive strategies involve fabrication of anisotropic surfaces with chemical or structural gradients, which provide the capillary driving forces for transporting droplets.[2,11−18] The passive strategies have the advantages of free energy input and simple device configuration, but they also encounter a few limitations, such as single functionality, low transportation speed, and short transportation distance.[13,14,19−24] In contrast, the active strategies, which utilize external stimuli such as mechanical vibrations,[25] magnetic fields,[26−28] electric fields,[23,29] heat,[30] sound, and light,[31−33] can be used for on-demand transportation of droplets. Electrowetting on dielectric (EWOD) is the most successful active strategy which has been widely used in designing liquid lenses, electrical paper, and digital microfluidic chips.[34] However, EWOD still suffers from poor long-term stability because of the electrical degradation and fouling of the hydrophobic dielectric layer. The requirement of high voltage, which may lead to the damage of biosamples, is another critical issue remaining to resolve for EWOD.[7] These problems may be circumvented using magnetic actuation, which is a remote, safe, and low-cost droplet transportation method.[35] Magnetic actuation of droplets can be realized using two distinct methods. The first method relies on the

Received: November 12, 2023
Revised: February 6, 2024
Accepted: February 8, 2024
Published: February 16, 2024

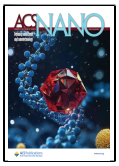

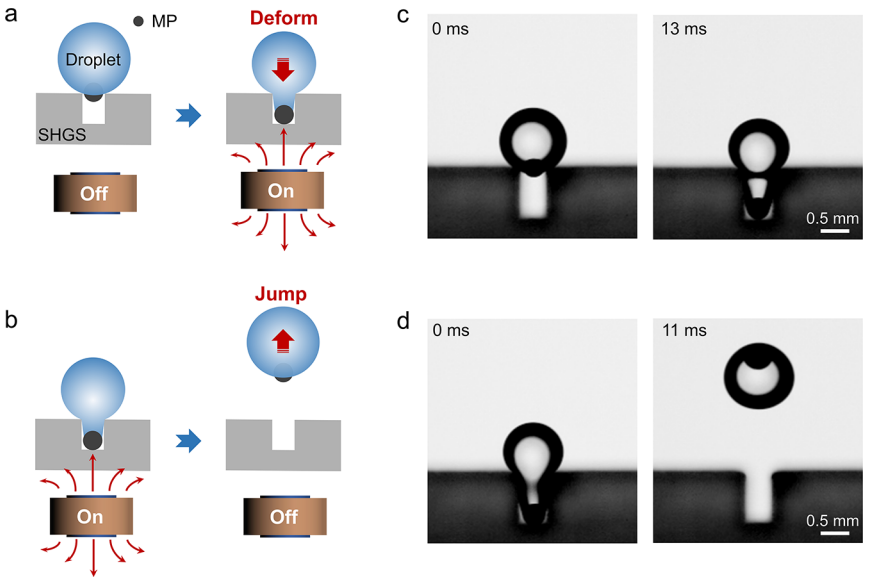

Figure 1. MAJ behavior. (a) When the electromagnet is switched on, the droplet with an attached MP is deformed on the SHGS. (b) When the electromagnet is switched off, the deformed droplet recovers its spherical shape and jumps on the SHGS. (c) The snapshots showing the deformation of the droplet when the electromagnet is switched on. (d) The snapshots showing the jumping behavior of the droplet when the electromagnet is switched off.

incorporation of magnetic particles (MPs) in the droplets. By exerting magnetic forces on the incorporated MPs, the droplets can be maneuvered.[26,27,36] The second method relies on the delicate design of the magnetoresponsive surfaces, whose morphologies can be tuned by the magnetic field, providing the structural anisotropy for droplet transportation.[28,37−39]

Conventional droplet transportation is performed on planar surfaces. To increase the throughput and flexibility, microfluidic platforms enabling three-dimensional (3D) droplet transportation are also emerging.[28,33,40,41] For example, Yuan et al. used ultrasonic tweezers to move the droplet across the steep slope and along the vertically placed convex surface.[33] Sun et al. realized spontaneous and fast transportation of droplets on a flexible and curved surface with printed surface charges.[20] In another work by Si et al., the 360° circular motion of a water droplet on the superhydrophobic copper circular orbit was achieved using magnetic actuation.[42] In the above examples, the droplets were merely transported on the nonplanar surfaces without leaving the surfaces. This droplet transportation mode can be referred to as in-surface 3D transportation. Compared to in-surface 3D transportation, out-of-surface 3D transportation of droplets is more difficult to realize due to the requirement of vertical actuation. For lifting the droplets from the supporting surfaces, the repulsive forces are usually required.[43] For instance, Li reported that a water droplet resting on the superhydrophobic surface was able to jump off the surface when an electrostatic tip, which introduced charges and provided electrostatic repulsion to eject the droplet, was positioned under the surface.[44] Alternatively, Mi et al. realized out-of-surface transportation of droplets on the superhydrophobic $LiNbO_3$:Fe crystal surfaces.[43] Under the focused laser illumination, the positive photovoltaic charges accumulated on the surfaces, resulting in repulsive electrostatic forces for lifting the droplets. These methods involve the use of a strong electric field and intense laser light, which may have adverse effects on the transported droplets. Up to date, to the best of our knowledge, out-of-surface 3D transportation of droplets using facile, safe, and low-cost actuation remains challenging.

To allow out-of-surface transportation of droplets, the adhesion forces of the droplets on the surfaces should be minimized. Therefore, the surfaces are usually rendered superhydrophobic for out-of-surface droplet transportation. In fact, on superhydrophobic surfaces, the droplet jumping phenomenon is ubiquitous, especially in humid environments where water vapor condenses on the surfaces.[45−50] When the tiny droplets merge together, the excess surface energy can partly convert to upward kinetic energy for droplet jumping. A single droplet may also jump spontaneously on the superhydrophobic surface which features a grooved structure.[48] When the droplet grows inside the superhydrophobic groove and evolves into a bulb shape, its upper surface possesses a larger radius of curvature compared to the bottom one, resulting in a Laplace pressure difference which acts as the driving force for droplet jumping. This phenomenon, from an energy aspect, is also caused by the conversion of excess surface energy to translational kinetic energy. Inspired by the spontaneous jumping behavior of droplets on the superhydrophobic surfaces, it would be useful to adopt the surface-energy-to-kinetic-energy jumping routine for out-of-surface transportation of droplets. However, it is still unresolved how to trigger the droplet jumping behavior on the superhydrophobic surfaces on demand, especially under the premise that the volume of the droplets should not be changed during transportation.

Herein, we introduce a versatile droplet transportation approach based on magnetic-actuated jumping (MAJ) of water droplets on the superhydrophobic grooved surfaces (SHGSs), which enables 3D, remote, and precise transportation of droplets. As shown in Figure 1a,b, MAJ refers to the behavior that the water droplet with an attached MP is capable of jumping on the SHGS when an electromagnetic pulse is applied. To elucidate the working mechanism of the MAJ behavior, the jumping dynamics are investigated via high-speed imaging and numerical simulation. It is revealed that the

https://doi.org/10.1021/acsnano.3c11197
ACS Nano 2024, 18, 6359−6372

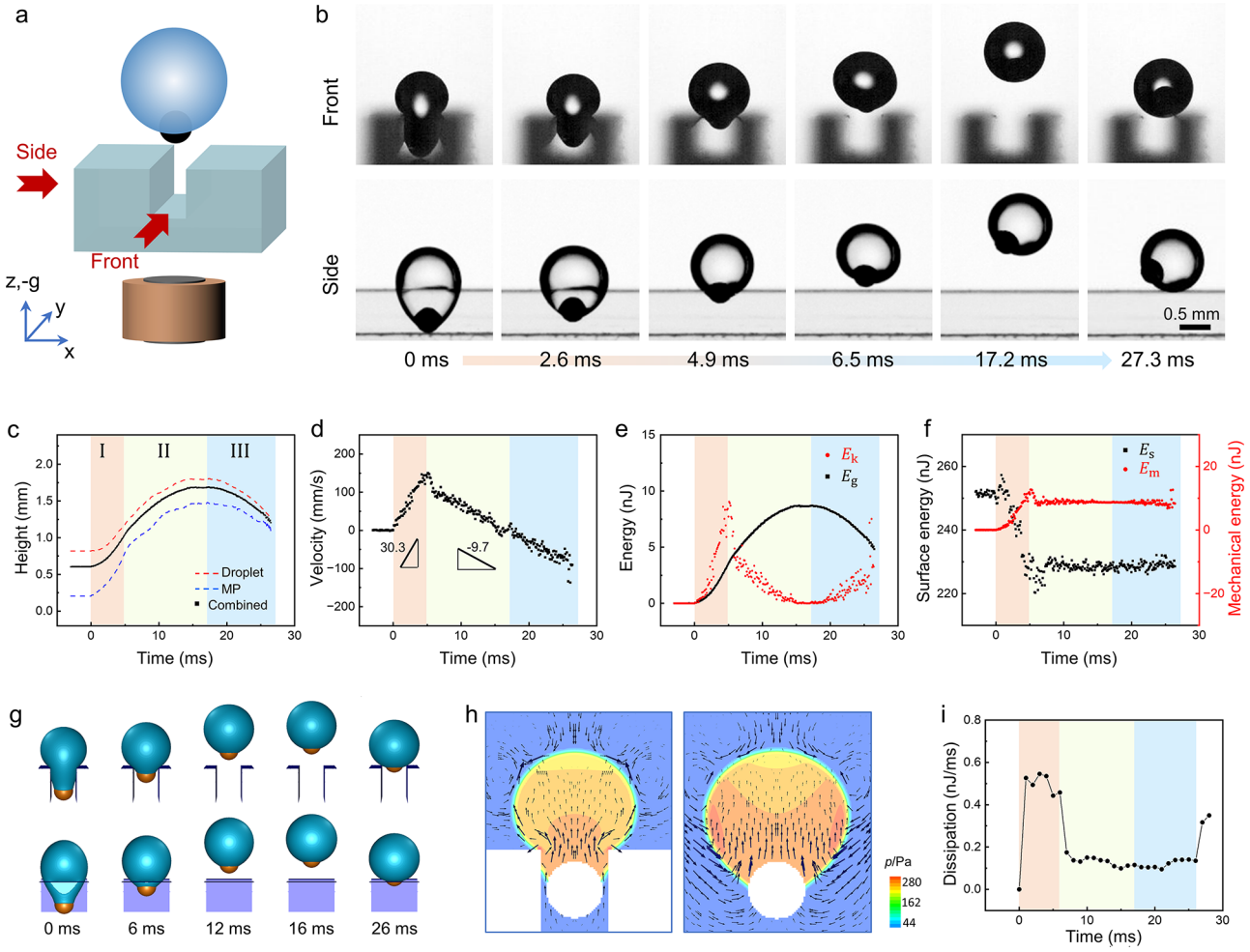

Figure 2. Understanding the MAJ behavior based on the jumping dynamics. (a) Schematic illustration of the experimental configuration for simultaneously capturing the front-view and side-view images of the droplet during MAJ. (b) Snapshots showing the MAJ behavior. The MP starts to move upward at the time of 0 ms when the electromagnetic field is removed. (c) The center-of-mass heights for the droplet, MP, and the combined droplet−MP system during MAJ. (d) The evolution of velocity of the droplet−MP system during MAJ. (e) The evolution of gravitational potential energy (E_g) and kinetic energy (E_k) of the droplet−MP system during MAJ. (f) The evolution of surface energy (E_s) and mechanical energy (E_m) of the droplet−MP system during MAJ. (g) Images showing the simulation results of the MAJ behavior. (h) The pressure contour inside the droplet, which is ejected from the superhydrophobic groove at 4 ms. The arrows indicate the flow field, and their lengths are proportional to the local velocities. (i) Viscous dissipation inside the droplet during the jumping process, which is obtained based on the simulated flow field.

electromagnetic field causes droplet deformation and increases the excess surface energy, which is partly converted into kinetic energy for droplet jumping when the electromagnetic field is quickly removed. Three motion modes of the droplets (*i.e.*, jumping, pinch-off and entrapment) during magnetic actuation are uncovered and understood based on the force and energy analyses. Besides being capable of in-surface and out-of-surface transportation of droplets, MAJ can be harnessed to transport droplets along complex trajectories, *e.g.*, climbing stairs and crossing obstacles. It is also suitable for droplet transportation in narrow and enclosed spaces. Therefore, MAJ serves as a highly desirable technique for 3D droplet transportation which can be implemented in a wide range of applications, such as bioassays, microfluidics, droplet-based switches, and micro-reactions.

RESULTS AND DISCUSSION

MAJ of Droplets on SHGSs. The grooved surfaces were prepared by 3D printing. They were intrinsically hydrophilic with a water contact angle of 75 ± 6° (Figure S1a). After being coated with a commercial superhydrophobic coating NeverWet, the surfaces became superhydrophobic with a water contact angle of 170 ± 5° and a sliding angle of 6 ± 2° (for 1-μL droplets). This low-surface-energy coating endows the surfaces with nanoscale roughness (Figure S1b), which enables air to be trapped at the solid−water interface and contributes to the extreme water repellency. A water droplet can be suspended on top of the superhydrophobic groove, which has a typical width of 0.55 mm (Figure S2). When a MP with a diameter of ∼0.4 mm is introduced into the droplet, it attaches to the liquid surface and settles at the bottom of the droplet (Figure 1c, left panel). Only a small portion of the MP protrudes outside the droplet due to its hydrophilicity (advancing contact angle = 50 ± 8°, receding contact angle = 28 ± 2°, see Figure S3 for the method to determine the contact angles of water on the MPs).

On the SHGS, the water droplet with an attached MP can be manipulated using an electromagnet 3 mm beneath the SHGS.

https://doi.org/10.1021/acsnano.3c11197
ACS Nano 2024, 18, 6359−6372

When the electromagnet is switched on, a magnetic field (strength ≈ 35 mT, gradient ≈ 13 T/m, Figure S4) emerges and acts on the MP, pulling it into the groove. Meanwhile, the droplet deforms and evolves into a bulb shape due to the confinement of the superhydrophobic groove and the adhesion of the MP (Figure 1c). When the electromagnet is switched off, the magnetic force acting on the MP vanishes. Without the magnetic attraction, the MP is pulled upward by the deformed water surface, which tends to recover to its original spherical shape. During this recovery process, the droplet can depart from the SHGS and show a MAJ behavior (Figure 1d). The symmetric structure of the square groove enables the droplet to undergo vertical jumping.

Mechanism of MAJ. To understand the mechanism of MAJ, we used two synchronized high-speed cameras to simultaneously capture the front-view and side-view images of the droplet during the jumping process (Figure 2a). Since the 3D-printed grooved surfaces showed poor transparency, for better visualization of the droplet in the groove, we used a transparent SHGS with similar dimensions and superhydrophobicity (width ≈ 0.55 mm, depth ≈ 0.7 mm, water contact angle = 165 ± 4°) for the mechanistic study. The transparent SHGS was constructed by assembling laser-cut glass slices and coated with a transparent superhydrophobic coating (see Figure S1c for the surface morphology and water contact angle, Figure S5 for the construction). Figure 2b gives the snapshots showing the jumping dynamics of a 0.53-μL water droplet on the SHGS. Before jumping (0 ms), the droplet shows a bulb shape in the front view. On top of the groove, the droplet only contacts the two edges of the groove without expanding laterally. This is consistent with the Gibbs criterion that the three-phase contact line is pinned at the edge when the local contact angle (∼140° at 0 ms) is smaller than the advancing contact angle, which approaches 180° for the superhydrophobic surface.[51,52] In the sideview, the droplet appears larger than that in the front view, indicating that the deformed droplet is extended along the groove. After the droplet departs from the groove, the front-view and side-view images of the droplet appear similar in both size and shape, indicating that without the confinement of the groove the droplet recovers to be spherical.

The jumping process can be divided into three sequential stages depending on whether the droplet is in direct contact with the groove and whether it reaches the maximal height. In stage I (0−4.9 ms), as soon as the electromagnet is switched off, the magnetic force vanishes and the droplet together with the MP is expelled from the groove. In this stage, the deformed droplet rapidly recovers its spherical shape and moves upward. In stage II (4.9−17.2 ms), the droplet completely detaches from the groove and continues its upward motion before it reaches the maximal height. In stage III (17.2−27.3 ms), the droplet eventually falls down before it impacts on the SHGS.

Based on the recorded images, we calculated the surface area of the droplet, and determined the center-of-mass heights for the droplet and the MP (detailed analysis is provided in the Experimental Section and Supporting Information, Figure S6). Figure 2c and d present the center-of-mass heights of the droplet−MP system and its velocity as functions of time during the jumping process. In stage I, both the center-of-mass height and the velocity keep increasing (the upward direction is defined as positive, see the coordinate system given in Figure 2a). In stage II, the center-of-mass height increases while the velocity decreases. The system reaches the maximal height at 17.2 ms when the velocity becomes 0. In stage III, the center-of-mass height decreases with an increased downward (negative) velocity. The downward acceleration in stage II and III is ∼9.7 m/s^2, being close to the acceleration of gravity. This implies that after the droplet detaches from the groove, gravity is the dominating force acting on the droplet−MP system. In contrast, in stage I, the average upward acceleration is ∼30.3 m/s^2, corresponding to an upward force of 24 μN acting on the droplet−MP system. As depicted in Figures S7 and S8, the upward force acting on the droplet−MP system is exerted by the top edges of the superhydrophobic groove. It is the force that appears to be counteracting the compression force at the groove edges by the deformed droplet with a bulb shape (detailed discussion on the driving force for MAJ is given in the Supporting Information (Additional Discussion I)).

The MAJ behavior can also be understood in terms of energy conversion. Based on the center-of-mass height h and velocity v of the droplet−MP system (total mass m), the gravitational potential energy ($E_g = mgh$ where g is the acceleration of gravity), translational kinetic energy ($E_k = 0.5mv^2$), and the overall mechanical energy ($E_m = E_g + E_k$) can be obtained. The liquid−vapor interface area A_{LV} can also be used to calculate the surface energy ($E_s = \gamma A_{LV}$, where γ is the surface tension of water). As shown in Figure 2e and f, the gravitational potential energy, translational kinetic energy, and the mechanical energy increase in stage I, while the surface energy decreases. This manifests that the surface energy is partly (≈ 30%) converted into the mechanical energy when the droplet is ejected from the groove. Afterward, the gravitational potential energy increases in stage II but decreases in stage III, while the kinetic energy shows opposite changes (Figure 2e). Their summation, *i.e.*, the overall mechanical energy, remains constant in stages II and III, indicating the conservation of mechanical energy. This is expected since in these two stages gravity is the only force acting on the system (ignoring air friction). According to the energy analysis, the MAJ behavior can be understood as follows: when the electromagnetic field is present, the droplet is deformed in the groove and thereby gains excess surface energy; when the electromagnetic field is quickly removed, the excess surface energy is released and partly converted into mechanical energy, including the translational kinetic energy for droplet jumping and the gravitational potential energy for height increment.

To better understand the MAJ behavior from a hydrodynamic point of view, we also performed numerical simulations to study the flow field inside the droplet during the jumping process. In the simulation, when the initially deformed droplet with an attached MP was allowed to move freely on the SHGS, a similar droplet jumping behavior was observed (Figure 2g). As depicted in Figure 2h, during the ejection process, the liquid inside the groove flows upward faster than that outside the groove, leading to bursting of the droplet above the groove (*i.e.*, expansion of the droplet bulb). This velocity difference also results in the transfer of upward momentum from the bottom of the droplet to the top, facilitating jumping of the entire droplet. In addition, it is evident that the pressure inside the droplet is inhomogeneous. The liquid inside the groove has a relatively larger pressure compared to the liquid outside the groove. This is due to the fact that the bottom liquid−vapor interface confined in the groove possesses a smaller radius of curvature, leading to a larger Laplace pressure ($\Delta p = \gamma(1/R_1 + 1/R_2)$ where R_1 and R_2

https://doi.org/10.1021/acsnano.3c11197
ACS Nano 2024, 18, 6359−6372

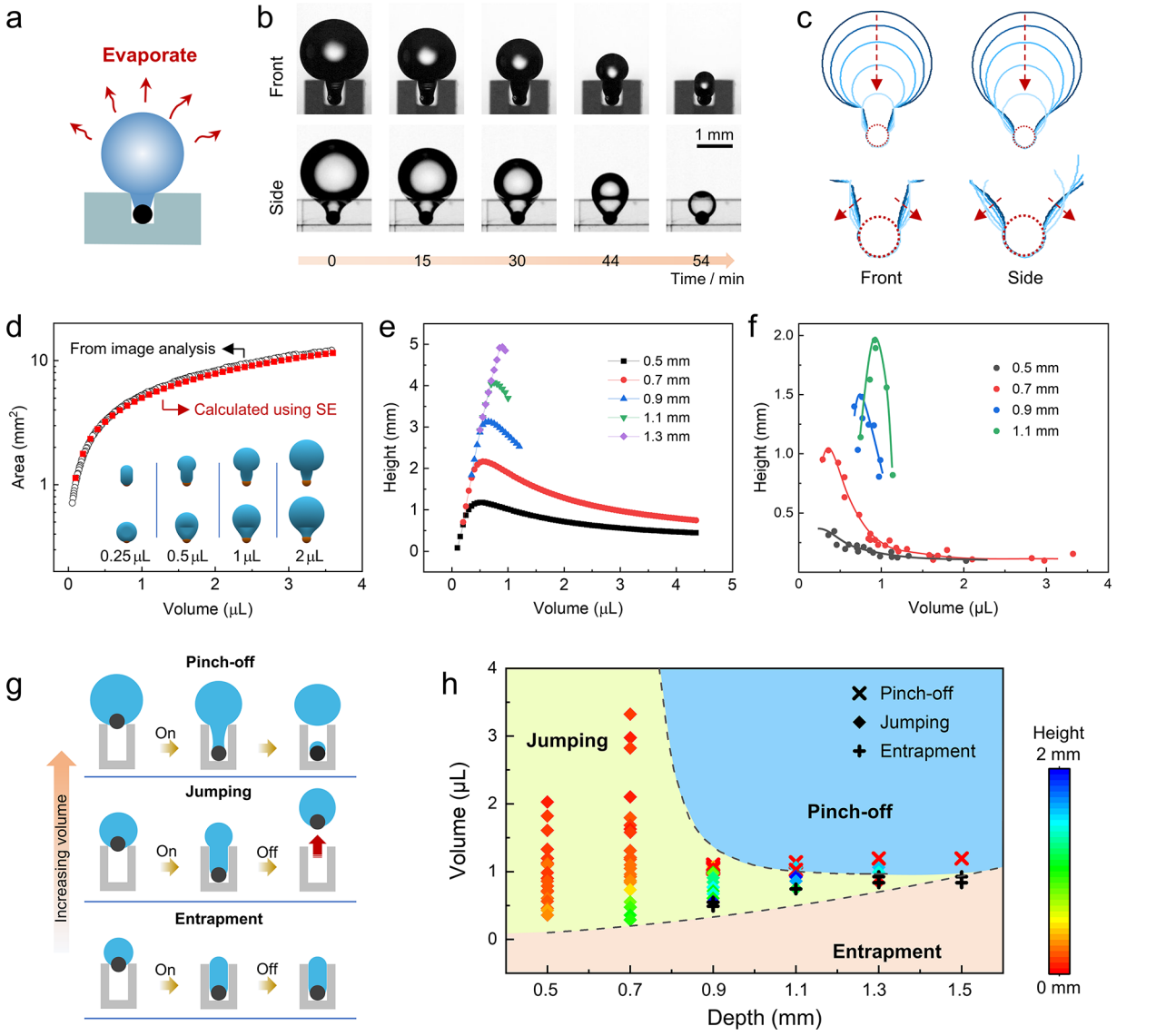

Figure 3. Influence of groove dimension and droplet volume on the MAJ behavior. (a) Illustration of the evaporation experiment which allows the deformed droplet to slowly decrease its volume. (b) Images of the deformed droplet during evaporation. The depth of the groove is 0.7 mm, and the width is 0.55 mm. (c) Profiles of the deformed droplet during evaporation. The bottom panels show the enlarged images of the droplet in the groove, and the arrows indicate the change of liquid−vapor interface. (d) Comparison between the surface areas of the deformed droplets from image analysis and from SE calculation. The insets show the droplet shapes obtained from SE calculation. (e) Theoretical jumping heights of the deformed droplets on the SHGSs with different groove depths. (f) Experimentally measured jumping heights of the deformed droplets on the SHGSs with an identical groove width of 0.55 mm but different groove depths. The lines are guides for the eyes. (g) Schematic illustration of the three motion modes of the droplets on the SHGS under magnetic actuation. (h) Regime diagram for the three motion modes. The curve demarcating the jumping and entrapment regimes is a plot using eq 2, while the curve demarcating the jumping and pinch-off regimes is obtained via SE calculation. The SHGSs have an identical groove width of 0.55 mm but different groove depths. The data points are obtained from experiments, and the color indicates the jumping height.

are the principal radii of surface curvature, being positive for a convex surface).[53] The resultant Laplace pressure difference, which acts as the internal driving force for expelling the liquid out of the groove, becomes more evident when the droplet bulb expands, since the radius of curvature for the top liquid−vapor interface increases during expansion.

Based on the flow field, the viscous dissipation rate inside the droplet during the jumping process can be calculated using the integral $\int_0^{\Omega} \phi \, d\Omega$, where Ω is the volume of the droplet and ϕ is obtained by[54]

$$\phi = \eta\left[2\left(\frac{\partial u}{\partial x}\right)^2 + 2\left(\frac{\partial v}{\partial y}\right)^2 + 2\left(\frac{\partial w}{\partial z}\right)^2 + \left(\frac{\partial u}{\partial y} + \frac{\partial v}{\partial x}\right)^2 + \left(\frac{\partial v}{\partial z} + \frac{\partial w}{\partial y}\right)^2 + \left(\frac{\partial w}{\partial x} + \frac{\partial u}{\partial z}\right)^2\right] \quad (1)$$

Here, (x,y,z) is the position vector, (u,v,w) is the velocity vector, and η is the viscosity of water. Figure 2i shows that the strongest viscous dissipation ($\approx$ 0.5 nJ/ms) is present in stage I when the droplet is ejected from the groove, reflecting the fact that flow inside the narrow groove causes severe viscous

https://doi.org/10.1021/acsnano.3c11197
ACS Nano 2024, 18, 6359−6372

dissipation. After the droplet departs from the surface, the viscous dissipation decreases to a low value (≈ 0.1 nJ/ms). This small but lasting viscous dissipation should be related to the shape oscillation of the droplet, which can be observed by the prolate−oblate shape transition during jumping (Figure S9a), and by the change of separation between the mass centers of the droplet and the MP (Figure S9b). Therefore, in a MAJ process, the excess surface energy is not only converted into the mechanical energy but also dissipated by viscosity and partly converted into the energy for shape oscillation.

Size Matching Effect for MAJ. By analyzing the jumping dynamics of the droplet on the SHGS, it has been revealed that the excess surface energy, which is positively correlated with the surface deformation of the droplet, provides the driving force for droplet jumping. In this section, we explore how to promote droplet deformation and jumping on the SHGSs by rational design of the groove. For this purpose, the influence of groove dimension and droplet volume on the droplet deformation needs to be investigated.

First, we fix the dimension of the groove (0.55 mm width, 0.7 mm depth) and evaluate the influence of droplet volume on the surface deformation of the deformed droplets on the SHGS. To successively change the droplet volume, a 3.6-μL deformed droplet on the SHGS was allowed to evaporate (Figure 3a). As shown in Figure 3b, the shape of the deformed droplet changes over time as its volume decreases. It can be observed that the upper portion of the droplet outside the groove is getting smaller when the volume decreases, while the lower portion inside the groove becomes thicker (Figure 3c). The enlarged images in the bottom panels of Figure 3c show that the bottom liquid−vapor interface becomes more convex as the volume decreases. This is indicative of a larger Laplace pressure inside the droplet. In fact, inside a small static droplet whose size is smaller than the capillary length (2.7 mm for water), regardless of surface deformation, the Laplace pressure should be equal everywhere, otherwise the pressure difference would cause internal flow.[55] As the radius of curvature for the top interface decreases during evaporation, the Laplace pressure inside the droplet increases. With an increased Laplace pressure, the bottom vapor−liquid interface expands and becomes more convex.

To quantify the surface deformation, we also use Surface Evolver (SE, an interactive program for evolving the surface toward minimal energy by the gradient descent method) to calculate the static shapes of the droplets when they are partly confined by the superhydrophobic groove and stick to the MP.[56] As shown in Figure 3d, the shapes of droplets from SE calculation appear similar to those obtained from experiments, and the areas of liquid−vapor interface from SE calculation and experiment (via image analysis) are well matched, within 5% discrepancy. Therefore, SE can be used for studying the surface deformation and excess surface energies of the deformed droplets on the SHGSs.

With the aid of SE, it is feasible to obtain the undeformed shapes of the droplets without being confined by the groove (Figure S10). Based on the liquid−vapor and liquid−solid interface areas of the droplet before and after deformation, we extract the excess surface energy ΔE_s for the deformed droplet on the SHGS (Figure S11a,b). Assuming ΔE_s is completely converted into mechanical energy, the theoretical jumping height H_j^* of the droplet can be calculated by $H_j^*=\Delta E_s/mg$. The theoretical jumping heights are plotted as functions of droplet volume in Figure 3e for the SHGSs with identical width (0.55 mm) but different depths (0.5−1.3 mm). Interestingly, for a specific SHGS, the theoretical jumping height shows an increasing tendency at small droplet volumes; when the droplet volume exceeds a critical value, the jumping height decreases with increasing volume. This phenomenon can be explained by the fact that, for large droplets, only a small portion of the droplet is deformed in the groove, therefore ΔE_s increases slowly with increasing volume (Figure S11b). As a result, the theoretical jumping height, *i.e.*, $\Delta E_s/mg$, decreases at large volumes. For small droplets, since they are more constrained by the groove, ΔE_s increases quickly with increasing volume, therefore $\Delta E_s/mg$ increases at small volumes. A similar tendency is also observed in the experiments (Figure 3f). For instance, on the SHGS with a depth of 0.7 mm, the maximal jumping height is experimentally observed at a volume of ∼0.4 μL, close to that obtained from theoretical calculations (0.55 μL). These two critical volumes are slightly different, because the theoretical calculation does not consider the dynamic effects, such as viscous dissipation and energy conversion efficiency, which also play important roles in determining the jumping height.

In general, the droplet jumps higher on the SHGSs with deeper grooves, since the droplet can have a larger deformation and gain more excess surface energy. However, this is only true in a certain range of droplet volume. If the volume is too small, the tiny droplets may entirely enter the groove and show a pancake shape. In this case, increasing the groove depth would not change the droplet shape and the theoretical jumping height (see the H_j^* vs volume curves in Figure 3e, which tend to overlap at small volumes). In fact, these tiny droplets are incapable of jumping due to entrapment, as illustrated in the bottom panel of Figure 3g. When the local contact angle of the droplet on the top surface of the groove is smaller than 90° (Figure S12), there is no upward driving force for droplet jumping, therefore the tiny droplets are entrapped in the groove. The critical volume V_e below which the droplet is entrapped in the groove can be calculated by subtracting the included volume of the MP inside the droplet ($V_{p,in}$) from the volume of the droplet pancake ($V_{pancake}$):

$$V_e = V_{pancake} - V_{p,in} = \frac{1}{24}\pi W(6L^2 + 4W^2 + 3\pi LW) - V_{p,in} \quad (2)$$

where L ($= D - 0.5W - L_{out}$) is the contact length of the droplet pancake in the groove, D and W are the depth and width of the groove, and L_{out} is the exposed length of the MP outside the droplet. L_{out} and $V_{p,in}$ are correlated with the dimensions of the groove as well as the contact angle of water on the MP (Figure S12).

On the other hand, if the droplet volume is too large, the pinch-off phenomenon is observed on the SHGSs with large depths (Figure S13). When the MP is pulled downward into the deep groove, the liquid connecting the MP and the droplet is elongated. The elongated capillary bridge eventually pinches off due to Plateau-Rayleigh instability, leading to separation of the MP from the droplet.[57,58] After pinch-off, the droplet cannot be transported using the electromagnetic field; therefore pinch-off should be avoided when MAJ is used for droplet transportation.

According to the above discussion, it can be concluded that size matching between the droplet and the groove is essential for efficient MAJ. Figure 3h presents the regime diagram

https://doi.org/10.1021/acsnano.3c11197
ACS Nano 2024, 18, 6359−6372

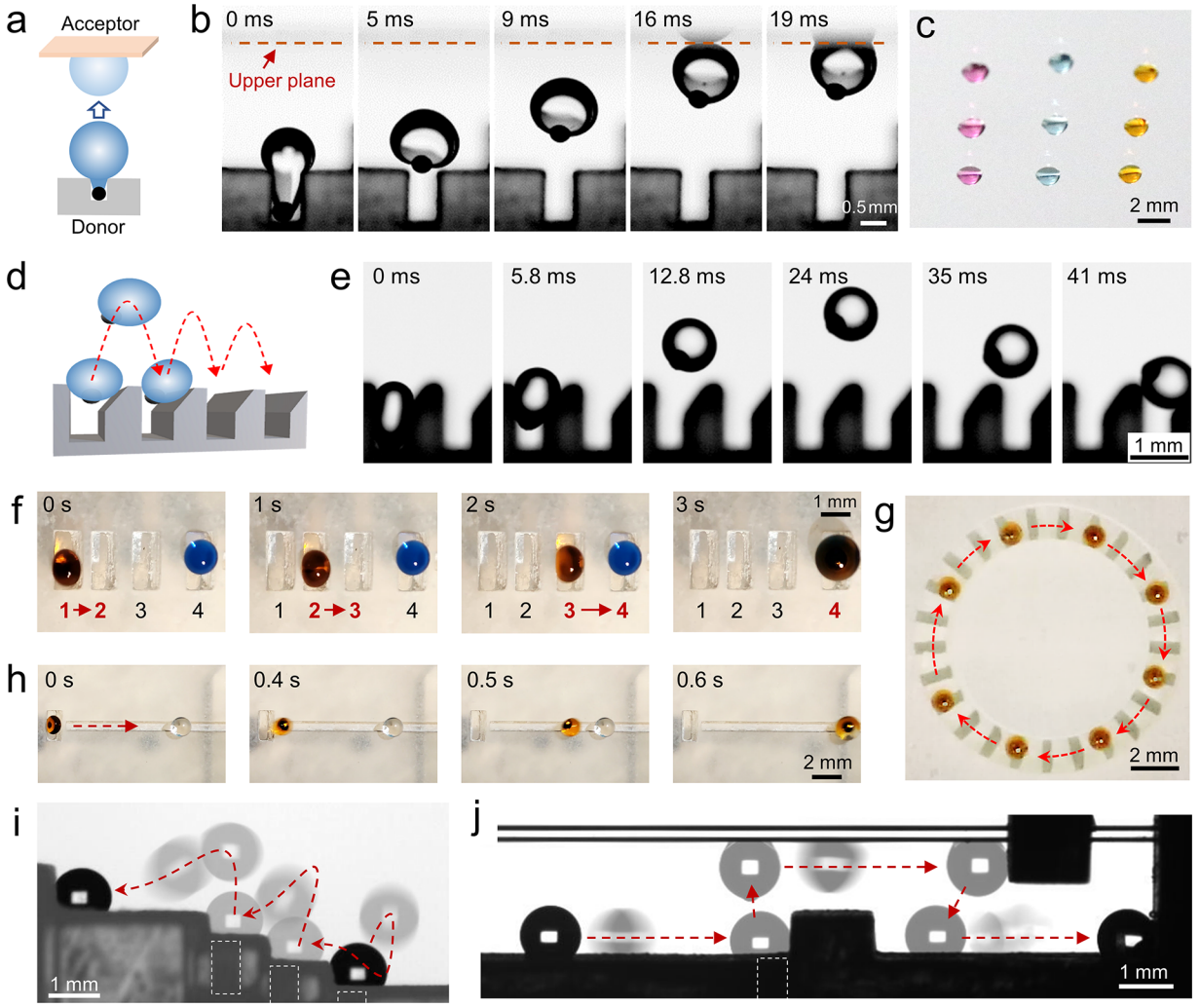

Figure 4. 3D droplet transportation based on MAJ. (a, b) Schematic illustration and snapshots showing the out-of-surface transportation of a droplet on the SHGS. (c) An image showing the multiple droplets which were transported to the acceptor surface at once using MAJ. (d, e) Schematic illustration and snapshots showing the directional transportation of a droplet on the chamfered SHGS. (f) Directional droplet transportation on the SHGS with multiple chamfered grooves. (g) A time-lapse image showing the directional transportation of a droplet on the SHGS with circularly arrayed chamfered grooves using MAJ. (h) Directional droplet transportation along the superhydrophobic track in front of the superhydrophobic chamfered groove. (i) Time-lapse trajectory of a droplet with an attached MP climbing the stairs based on MAJ. (j) Time-lapse trajectory of a droplet with an attached MP crossing obstacles using MAJ. The arrows in i and j indicate the trajectories of the droplets while the dashed rectangles indicate the positions of the grooves.

summarizing the three motion modes (*i.e.*, jumping, entrapment, and pinch-off) of droplets on the SHGSs with an identical groove width of 0.55 mm but different groove depths under magnetic actuation. The curve demarcating the jumping and entrapment regimes is a plot using eq 1, while the curve demarcating the jumping and pinch-off regimes is obtained via SE calculation (details are given in the Experimental Section). The experimental results prove the validity of the regime diagram. It is evident that the jumping regime is relatively broad at small depths (≤0.9 mm), but it becomes narrower with increasing the depth of the groove. Thus, if the SHGSs are used for transporting droplets with a wide range of volume, relatively shallow grooves should be designed (*e.g.*, depths in the range of 0.7−0.9 mm). On the contrary, if the SHGSs are used for transporting droplets for a long distance, the deep grooves (depths in the range of 0.9−1.3 mm) are more suitable. It is noteworthy that the SHGSs with very deep grooves (*e.g.*, depth >1.5 mm in Figure 3h) cannot be used for MAJ because failure due to either entrapment or pinch-off is inevitable for all droplets. The SHGSs with depths ≤ 0.5 mm may also be inapplicable owing to the small jumping heights.

In fact, apart from the groove depth, the groove width also has significant effect on the MAJ behavior. As demonstrated in Figure S14a and b, increasing the groove width leads to increments of the critical volume and critical depth for pinch-off. The critical volume for entrapment also increases with groove width, though the increment is small compared to that for pinch-off. As a result, the jumping regime becomes broader when the groove width is increased. The theoretical jumping height of a droplet on the SHGS decreases with increasing groove width (Figure S14c), because the droplet is less deformed and has less excess surface energy for jumping on the broader SHGS. The regime diagram for the three motion modes of droplets on the SHGSs with an identical groove depth (0.9 mm) but different widths is presented in Figure S14d. It shows that the MAJ behavior can only be obtained at intermediate groove widths, since the pinch-off (or entrapment) effect would be observed if the width is too small (or

https://doi.org/10.1021/acsnano.3c11197
ACS Nano 2024, 18, 6359−6372

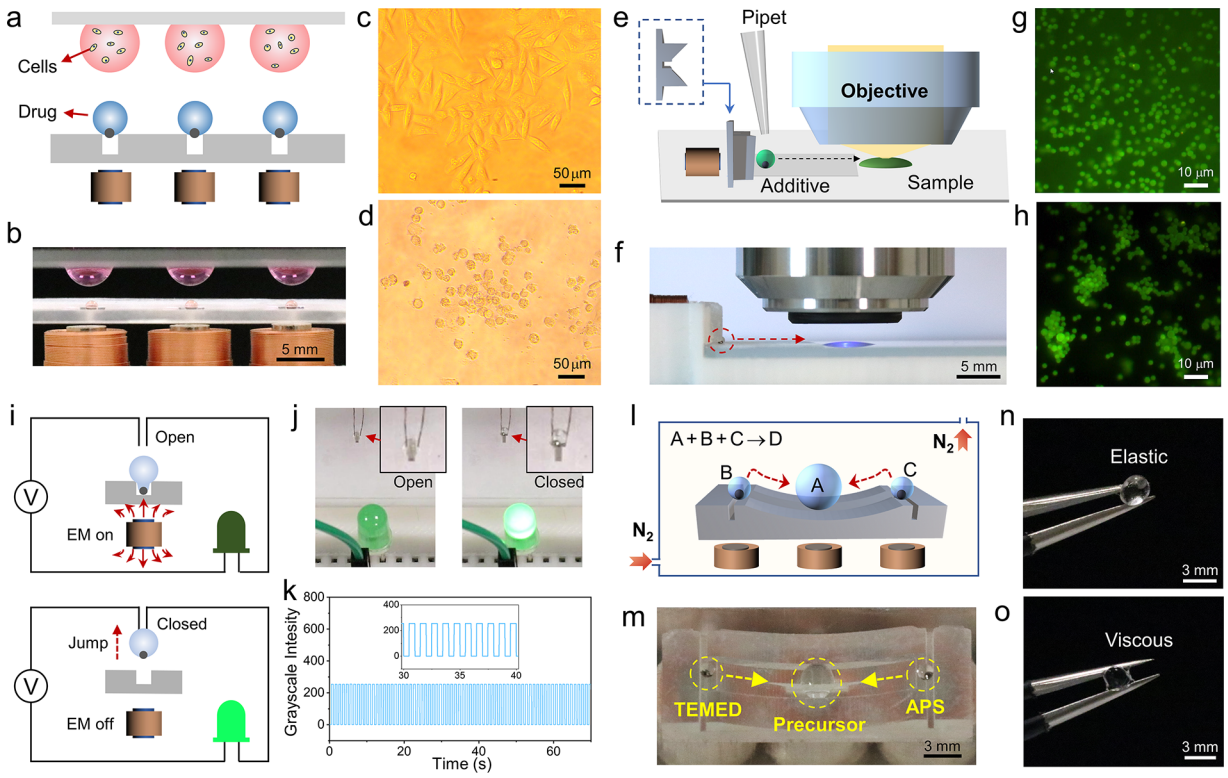

Figure 5. Applications of MAJ. (a, b) Schematic and image showing the experimental setup for remotely delivering the drug droplets to the hanging cell droplets using MAJ. (c,d) Bright-field microscopic images showing the cell morphology without (c) and with (d) adding the drug. (e,f) Schematic and image showing the transportation of an additive droplet to the sample under the microscope. (g,h) The fluorescent microscopic images showing the dispersion states of the colloidal particles in water before (g) and after (h) adding electrolytes. (i) Schematic illustration of the droplet-based switch using MAJ. (j) Images showing the switch in the open and closed states, respectively. The enlarged images show the location of the conductive droplet. (k) Intensity of the light as a function of time when the switch is repeatedly turned on and off. (l,m) Schematic and image showing the microreaction platform in a closed chamber. Using MAJ, it is feasible to remotely add reactants for the microreaction without the need to open the chamber. (n) The as-synthesized hydrogel appears elastic when the microreaction is performed in the enclosed chamber with N_2 protection. (o) The as-synthesized hydrogel is viscous and sticky if the chamber is open and the reaction is performed in the air.

too large). The theoretical jumping height for a droplet with a given volume increases with decreasing the groove width and/or increasing the groove depth (Figure S15). Thus, for long-distance transportation of droplets, under the premise that the pinch-off effect can be prevented, SHGSs with relatively narrow and deep grooves should be used. Further discussions about the influences of MP size, groove shape, and surface hydrophilicity of the MPs on the MAJ behavior are given in the Supporting Information (Additional Discussion II, Figures S16–S18).

Droplet Manipulation Based on MAJ. Based on the MAJ behavior, the SHGSs can be used for out-of-surface transportation of droplets (Figure 4a). For example, as shown in Figure 4b, when a glass slide acting as an acceptor was placed 2.5 mm above the SHGS (0.9 mm depth, 0.55 mm width), a 1-μL water droplet was able to be transferred from the SHGS to the acceptor surface via MAJ. After transfer, the droplet did not fall down under gravity because of the adhesion force between the droplet and the acceptor surface. The MP inside the transferred droplet could be separated by applying another electromagnetic pulse (Figure S19). On the SHGS with multiple grooves, it is also possible to transfer multiple droplets to the acceptor surface at the same time using a single electromagnetic pulse (Figure 4c and Figure S20).

Apart from achieving out-of-surface transportation of droplets, MAJ can also be used for in-surface transportation of droplets on the SHGS. For this purpose, one edge of the groove should be chamfered to control the jumping direction (Figure 4d, the detailed dimensions of the chamfered groove are given in Figure S21a). As shown in Figure 4e, when being ejected from the chamfered groove, the droplet expands to the chamfered side and acquires the momentum for oblique jumping toward the right. The oblique jumping behavior can be understood through force analysis. In the squared groove, the droplet is squeezed symmetrically by the side walls of the groove (Figure S7a); however, in the chamfered groove, the droplet is less squeezed by the chamfered wall (Figure S21b,c). As a result, the droplet is pushed to the chamfered side during the jumping process. The size matching effect is also observed for MAJ on the chamfered SHGS. Only the droplets with volumes in the range of 0.4–0.8 μL can jump out of the chamfered groove (0.55 mm width, 1.3 mm depth, 0.6 mm chamfered depth, 0.4 mm chamfered length) and exhibit forward motion, as demonstrated in Figure S21d,e. The smaller droplets are entrapped in the groove, while the larger droplets cannot jump forward on the chamfered groove due to their limited horizontal displacements during MAJ.

Utilizing the directional MAJ behavior, various directional transportation modes can be realized. Figure 4f presents that on the SHGS with four chamfered grooves, the orange droplet (dyed with methyl orange, 1.3 μL) was sequentially transported from the first groove to the fourth groove and

https://doi.org/10.1021/acsnano.3c11197
ACS Nano 2024, 18, 6359–6372

eventually merged with the blue droplet (dyed with Coomassie brilliant blue, 1.3 μL) at the fourth groove. In Figure 4g and Movie S1, the circular droplet motion was realized on the SHGS with circularly arranged chamfered grooves. It can be seen that the trajectory of the transported droplet is determined by the arrangement of the chamfered grooves, while the transportation distance can be precisely controlled by the electromagnetic pulses. Figure 4h presents another configuration for in-surface transportation of droplets using chamfered grooves. It shows that the orange droplet jumped out from the chamfered groove and slid along the sliding track for a long distance before mixing with the aqueous droplet on the track. The sliding track not only directed the motion of the droplet but also decreased the friction, since it enabled the MP to be suspended below the sliding droplet without touching the bottom of the track. Unlike the stepwise transportation of droplets on the SHGSs with multiple chamfered grooves, the transportation of droplets along the track is continuous.

By leveraging an additional magnetic field for controlling the moving direction, more complex 3D transportation of the droplets, *e.g.*, climbing stairs and crossing obstacles, can be achieved using MAJ. As shown in Figure 4i and Movie S2, the 0.9-μL droplet incorporated with a MP was capable of climbing the stairs. Actuated by an electromagnetic pulse, the droplet jumped out of the groove on the lower stair. During jumping, it was driven to move leftwards by the permanent magnet located on the left of the stairs (Figure S22a). Therefore, the droplet was transferred to a higher stair after each electromagnetic pulse. In Figure 4j and Movie S3, the 0.9-μL droplet was able to cross the obstacles under magnetic actuation. For this manipulation, two electromagnets were required, one on the right to drive the rightward motion of the droplet, and another beneath the bottom surface for triggering MAJ (Figure S22b). First, the droplet with an attached MP was located on the bottom surface. When the electromagnet on the right was switched on, the droplet was driven to move to the right before being blocked by the obstacle. After the electromagnet on the right was switched off, an electromagnetic pulse was applied by the bottom electromagnet to trigger droplet jumping on the groove behind the obstacle. The droplet jumped and attached to the upper surface above the obstacle (a low-adhesion capillary tube coated with perfluoropolyether was used to provide the upper surface, see Note S1 in the Supporting Information). Later, it was driven to move along the upper surface to the right before it encountered another obstacle on the upper surface. The droplet was then transferred back onto the bottom surface using the bottom electromagnet. At last, it was moved rightwards to the destination using the right electromagnet.

From the above demonstration, it can be seen that MAJ offers a versatile strategy for multidimensional transportation of droplets. Compared to other magnetic transportation strategies, MAJ-based droplet transportation is reliant on the modulation of the electromagnetic field. It has an advantage that no moving mechanical parts are required in the entire transportation setup, facilitating the design of miniaturized fluidic platforms. MAJ holds great promise for various applications, which will be presented in the following section.

Applications Based on MAJ. Thanks to the capability for precise, remote, and multidimensional transportation of droplets, MAJ can be used to transfer microliter droplets in confined and narrow spaces where a traditional pipet method is inapplicable. As a proof of concept, we used MAJ to deliver drugs to the hanging cell droplets, see Figure 5a,b and Note S2. A similar hanging droplet configuration has been adopted for drug screening, in which accurate delivery of the drug into the cell droplets is required.[59] Our platform was comprised of a top glass slide with three circular holes for suspending the cell droplets (40 μL, MCF-7 cells cultured in Dulbecco's modified eagle medium (DMEM)), a middle substrate consisting of three superhydrophobic grooves for depositing and actuating the drug droplets (1.5 μL, 2.0 μM doxorubicin hydrochloride) with attached MPs, and the bottom electromagnets for triggering MAJ. When the electromagnetic pulses were applied by the electromagnets, the drug droplets jumped and merged with the cell droplets. To promote mixing, weak alternating magnetic fields were applied for 2 min to oscillate the MPs inside the droplets (if two MPs were added into one drug droplet, the oscillation could be enhanced). Afterward, the electromagnetic pulses were again applied to separate the MPs from the droplets. To prove that the drug droplets had been successfully delivered into the cell droplets, we transferred the cell droplets into 96-well plates for incubation and microscopic observation. Indeed, the drug droplets had been added into the cell droplets and decreased the cell viability, as evidenced by the high proportion of dead cells with a round morphology (Figure 5c, d).[60]

Apart from realizing out-of-surface delivery of droplets, MAJ can also be used to transport droplets along the surface even in a narrow space. For instance, in Figure 5e and f, a microscope is used for in situ observation of the aggregation process of colloidal particles at the water−air interface when the electrolyte is introduced. Usually, the sample should be removed from the microscope for adding the additive using a pipet. However, in this case, it is impossible to capture the aggregation process continuously because it takes time for reloading and refocusing the sample under the microscope. Here, using MAJ, we added a 0.9-μL additive droplet (sodium hydroxide, 50 wt %, Note S3) to the testing sample (0.1 wt % carboxylated polystyrene particles dispersed in water, particle diameter = 1.5 μm, volume = 6 μL) directly under the microscope, even when the separation between the objective and the sample was only 3 mm. To transporting the additive droplet along the surface (out-of-surface motion is undesired since the droplet may touch the objective), the SHGS and the electromagnet was positioned horizontally with the jumping direction pointing to the sample. The additive droplet with a MP was deposited in front of the SHGS using a pipet. *Via* MAJ, the additive droplet was ejected and slid along the superhydrophobic track before it merged with the sample. The microscopic behavior of the colloidal particles before and after adding the additive was recorded continuously under the microscope without interrupting. As shown in Figure 5g and h, the colloidal particles were initially well dispersed but agglomerated after adding the electrolyte, reflecting the fact that the electrical double layers surrounding the particles were compressed and the interparticle repulsive forces were minimized.[61]

Furthermore, the MAJ behavior can be used to design droplet-based switches which are responsive to magnetic fields. The working mechanism of the droplet-based switches is depicted in Figure 5i. When the magnetic field is present, the conductive droplet is deformed on the SHGS, and the outer circuit is open (light off, top panel in Figure 5i). As the magnetic field is quickly removed, the droplet jumps up and links the two conducting wires on top of the SHGS, resulting

https://doi.org/10.1021/acsnano.3c11197
ACS Nano 2024, 18, 6359−6372

in closure of the outer circuit (light on, bottom panel in Figure 5i). A droplet-based switch was fabricated following the procedures given in Note S4. Its open and closed states are presented in Figure 5j, which reveals that the switch is controlled by changing the location of the droplet using MAJ. This droplet-based switch showed good repeatability when it was cyclically switched on and off for more than 70 cycles (Figure 5k).

Last but not least, MAJ can be used to remotely control microreactions within enclosed chambers. As illustrated in Figure 5l, the microreaction platform is placed inside a nitrogen-filled closed chamber, which provides an oxygen-free environment for the reaction. The reagent droplets, *e.g.*, A, B (with a MP), and C (with a MP), are initially deposited on the specific positions with grooved structures on the platform. After the chamber is closed, using MAJ, the reagent droplets B and C can be triggered to jump and mix with the reagent droplet A for starting the chemical reaction. Since the reagents can be added and mixed without opening the chamber, unwanted introduction of oxygen can be efficiently prevented. We used this microreaction platform to fabricate poly(acrylamide) hydrogel. For this purpose, the tetramethylethylenediamine (TEMED) and ammonium sulfate (APS) droplets should be added into the acrylamide/bis-acrylamide precursor droplet (Figure 5m, Note S5).[62] After closing the chamber and degassing for 10 min, the APS and TEMED droplets were transferred to merge with the precursor droplet using MAJ (Movie S4). By periodically activating the two electromagnets on the sides, the merged droplet was mixed. After mixing, the MPs were separated from the droplet using the center electromagnet (a deep groove was located at the center of the platform, enabling the MPs to be separated from the droplet). After reacting for 1 h, we observed that the droplet was successfully transformed into an elastic hydrogel, see Figure 5n. In contract, if the chamber was open and the reaction was performed in air, the droplet was not completely cross-linked and appeared viscous after reaction (Figure 5o), since the radical polymerization reaction was inhibited by oxygen. These results verify the applicability of MAJ in microreactions which are performed in the enclosed environments.

CONCLUSIONS

In summary, 3D, remote, and precise transportation of droplets is realized using MAJ on SHGSs. Through high-speed imaging and numerical simulation, it is revealed that the MAJ behavior is governed by the conversion of excess surface energy to kinetic energy. The excess surface energy is gained when the droplet with an attached MP is forced to deform in the superhydrophobic groove under the electromagnetic field. The excess surface energy is partly converted into kinetic energy for droplet jumping when the electromagnetic field is quickly removed. It is found that size matching between the droplet and the groove is essential for efficient MAJ. If the sizes are not matched, unwanted entrapment or pinch-off effects would lead to failure of MAJ. To guide the design of SHGSs for MAJ, a regime diagram is proposed, which shows that the shallow SHGSs are preferable for transporting droplets with a wide range of volumes, while relatively deep SHGSs should be adopted to increase the transportation distance. The influence of groove structure on the jumping behavior is also demonstrated. Droplets jump vertically on the SHGSs with symmetric squared grooves but show an oblique jumping behavior on the chamfered SHGSs. Based on MAJ, various droplet manipulation modes are achieved, including out-of-surface and in-surface directional transportation, climbing stairs, and crossing obstacles. Serving as a versatile approach for droplet transportation in confined and enclosed spaces, MAJ holds great potential for numerous applications, including bioassay, microfluidics, droplet-based switches, and microreactions.

EXPERIMENTAL SECTION

Materials. The superhydrophobic coatings NeverWet and Glaco were purchased from Rust-Oleum Corporation and SOFT99 Corporation, respectively. UV sensitive resin (405 nm wavelength, clear) for 3D printing was purchased from Anycubic. The MPs (diameter ≈ 409 μm, mass ≈ 0.27 mg) were purchased from Ningyang Zhenjie steel ball factory. They were used after cleaning using acetone, alcohol, and Milli-Q water. Milli-Q water used in this study was produced using a Milli-Q IQ 7000 system. Acetone was purchased from Guangzhou Chemical Reagent Factory. Alcohol was purchased from GHTECH. Methylene blue trihydrate (98%), Coomassie brilliant blue (G250, Biotechnology grade), and APS were purchased from Macklin. Methyl orange (85%), acrylamide, and bis-acrylamide were purchased from Aladdin. Sodium hydroxide (98%) was purchased from General Reagent. TEMED, sodium chloride, and Rhodamine B (98%) were purchased from Adamas. DMEM was purchased from Solarbio. The 1.5-μm monodispersed fluorescent carboxylated polystyrene particles were purchased from Jiangsu Zhichuan Technology Co., Ltd. The optical adhesive (NOA61) was purchased from Norland.

Fabrication of the SHGSs. The UV sensitive resin was used to fabricate the SHGSs using a 3D printer (Photon Mono SE, Anycubic), which had a resolution of 51 μm in the *xy* plane and 10 μm resolution along the *z* direction. The samples were printed with a layer thickness of 50 μm. The exposure time for each layer was 1.5 s. The as-printed samples were intrinsic hydrophilic. They were coated using NeverWet following two steps. First, a thin layer of base coat which acted as a binder was sprayed on the surface. Second, the top coat with nanosized hydrophobic particles was sprayed on the surface to form a superhydrophobic layer. After each step, the coating was dried at ambient temperature for at least 30 min. For fabricating the transparent SHGS, the laser-cut glass slices were assembled and glued using the optical adhesive to form a groove with a width of 0.55 mm and a depth of 0.7 mm, see Figure S5 for the construction. The transparent superhydrophobic coating Glaco was sprayed on the groove, followed by drying at 70 °C for 30 min. Scanning electronic microscope (SEM) images of the coatings were recorded using Sigma 500 (Zeiss, Germany). The operation voltage was 2 kV.

Measurement of the Contact Angles. The contact angles of the samples were measured using a goniometer (Krüss, DSA100S). Typically, 5-μL aqueous droplets were deposited on the surfaces. The images of the sessile droplets were recorded, and the outlines were fitted based on the Young−Laplace model using the ADVANCE software (Krüss). For each surface, at least seven independent measurements were carried out to determine the contact angle. To measure the advancing and receding contact angles of water on the MPs, the water droplet was fixed by a metal ring, and the MP was brought to contact and compress the droplet at a constant speed of 0.1 mm/s using a linear motor (DDSM100/M, Thorlabs). Afterward, the MP was retracted with the same speed. A high-speed camera (VEO 710L, Phantom) was used to record the images of the droplet and the MP during compression and retraction, and the advancing and receding contact angles were extracted from the images (Figure S3).

Measurement of the Magnetic Field. The magnetic field around the electromagnet was measured using a Gauss meter (CH-1600, CH-Magnetoelectricity Technology).

Observation of the MAJ Behavior. After the droplet was dispensed onto the SHGS, a MP was introduced into the droplet. An electromagnet was positioned 3 mm below the SHGS to actuate the

https://doi.org/10.1021/acsnano.3c11197
ACS Nano 2024, 18, 6359−6372

droplet. The electromagnet was controlled by a signal generator (DG1062Z, Rigol) and a power amplifier (ATA-105, Aigtek). The high-speed camera equipped with a macro lens (100 mm/F2.8, Tokina) was employed to capture the MAJ process at a speed of 10 000 frames per second. To capture the front and side views of the droplet during MAJ, two high-speed cameras were arranged in an orthogonal configuration for simultaneous recording.

Image Analysis. The Matlab software was used for image analysis. We used the front-view and side-view images of the droplet on the transparent SHGS to extract its surface area and volume. Typically, the droplet can be divided into three portions, see Figure S6a. The top portion is outside the groove. The second and third portions are inside the groove. For the second portion, the liquid is in contact with the groove, while for the third portion the liquid is not in contact with the groove. For the first portion, we cut the droplet into horizontal slices, which have a thickness of one-pixel size (about 20 μm). Assuming the slice has an ellipse shape (Figure S6b), the long axis L and the short axis W can be measured from the side-view and front-view images, respectively. The area of the slice S is calculated using $S = \pi LW/4$. Multiplying the area by the thickness of the slice h^*, we obtain its volume. To calculate the outer surface area of the slice (*i.e.*, water-vapor interface area), we first calculate the perimeter of the ellipse p following:

$$p = \frac{\pi(L+W)}{2}\left(1 + \frac{1}{4}h + \frac{1}{64}h^2 + \frac{1}{256}h^3 + \frac{25}{16384}h^4 + \frac{49}{65536}h^5\right) \tag{3}$$

where $h = (L-W)^2/(L+W)^2$. Denoting the studied slice with the subscript 1 and a neighboring slice with the subscript 2, the slant height SH of the conical frustum (Figure S6c) consisting of these two slices can be calculated by

$$\mathrm{SH} = \frac{\sqrt{\frac{(L_2-L_1)^2}{4} + h^{*2}} + \sqrt{\frac{(W_2-W_1)^2}{4} + h^{*2}}}{2} \tag{4}$$

Thus, the outer surface area S_{out} of the studied slice can be approximated by

$$S_{out} = \frac{p_1 + p_2}{2}\cdot \mathrm{SH} \tag{5}$$

Summing up all slices, we obtain the volume and surface area for the first portion. For the second portion, each slice is divided into three parts—a rectangle and two half circles (Figure S6d). The area of the slice is calculated by $L_{contact}W + 1/4\pi W^2$, where $L_{contact}$ is the length of the rectangle (the interface between water and groove wall). Thus, the volume of the slice is $(L_{contact}\, W + 1/4\pi W^2)h^*$. The area of the water surface for each slide is calculated using $2L_{contact}\, h^* + \pi W\cdot \mathrm{SH}'$, where SH′ is obtained using

$$\mathrm{SH}' = \sqrt{\frac{(L_2-L_1)^2}{4} + h^{*2}} \tag{6}$$

For the third portion, the method to determine the volume and the outer surface is similar to that used for the first portion. However, the contribution from the MP should be subtracted. The subtracted volume is $\pi D^3/6$, where D is the diameter of the MP. The subtracted surface area is $\pi D L_{out}$, where L_{out} is the height for the exposed (unsoaked) portion of the MP.

Simulating the Jumping Behavior of the Deformed Droplet on SHGS. 3D numerical simulations were performed to study the jumping behavior of the deformed droplet with an attached MP on the SHGS. The governing equations (continuity and momentum equations) were solved using ANSYS Fluent software (version 19.0) with a pressure-based solver. The simulation was carried out using the Tianhe-2 supercomputer at the National Supercomputer Centre in Guangzhou (NSCC-GZ). In the simulation, the VOF (volume of fluid) method, laminar flow model, and no-slip boundary condition were adopted. The continuum surface force method was used to include the effect of surface tension, which served as the force source term in the momentum equation (Navier–Stokes equation). The second-order upwind scheme was used to discretize the momentum equation, and the coupled scheme was used for pressure–velocity coupling. The gravity acceleration was set as -9.8 m/s^2. The contact angles were 170° and 50° for the superhydrophobic walls and the MP (during jumping, the MP had a tendency to enter the droplet, therefore the contact angle was more close to the advancing contact angle). The surface tension of water was 0.072 N/m. An overset interface was used, enabling the movement of the MP under capillary and gravity forces. To obtain the original shape of the deformed droplet on the SHGS, the droplet contacting both the fixed MP (at the bottom of the groove) and the superhydrophobic groove was first simulated for 10 ms, resulting in a bulb shape similar to that observed in the experiment. The velocity field was set zero to mimic the static state. The deformed droplet was allowed to move freely on the SHGS when the position of the MP was not fixed (*i.e.*, when the overset meshed was set movable). A typical time step in the simulation was 0.01 ms.

Calculating the Equilibrium Shape of the Droplet Using SE. The energy minimization algorithm implemented in SE was used to study the static shape of the droplet when being confined by the SHGS and adhesive to the MP. In SE, the surfaces were presented by meshes consisting of triangular facets. The force vector at each vertex was calculated as the gradient of the total energy (g command). The commands r, u, and V were used for refining the mesh, equiangulation, and vertex averaging. In the calculation, water was partly confined in the SHGS, which was treated as ideally superhydrophobic (contact angle approaching 180°), while the contact angle for the MP was 28° (the experimentally determined receding contact angle of water on the MP; when the MP at the liquid–vapor interface is pulled into the groove, the contact angle is more close to the receding contact angle). The acceleration of gravity was set as 9.8 m/s^2 in the calculation. After the system reached the equilibrium state, the areas of the water surface (A_{LV}, including those in contact with the superhydrophobic walls) and the interface between water and the MP (A_{SL}) were recorded. They were used to calculate the surface energy E_S following:

$$E_S = \gamma(A_{LV} - A_{SL}\cdot\cos\theta) \tag{7}$$

where γ is the surface tension of water. We also simulated the equilibrium shape of the droplet without being confined by the groove and calculated the surface energy E_S^*. The excess surface energy was then obtained by $E_S - E_S^*$. To determine the critical height of the groove above which the pinch-off phenomenon was observed, we first simulated the equilibrium shape of the droplet on the SHGS with a small depth. Subsequently, the depth was increased step by step (step size = 0.005 mm). For each step, the equilibrium shape of the droplet was simulated. At the critical depth, the pinch-off phenomenon was observed, and the calculation became unstable and unphysical.

ASSOCIATED CONTENT

Supporting Information

The Supporting Information is available free of charge at https://pubs.acs.org/doi/10.1021/acsnano.3c11197.

Additional discussions; additional experimental methods; SEM images and contact angles of water on the 3D-printed planar surfaces with different surface coatings; water droplets suspending on the SHGS; the method used to determine the water advancing and receding contact angles on the MPs; magnetic field around the electromagnet (EM); construction of the transparent SHGS; image analysis to obtain the volume and liquid–vapor interface area of the deformed droplet on the SHGS; force analysis for the deformed droplet on the SHGS; exploring the maximal driving force for droplet jumping; shape oscillation of the droplet during

https://doi.org/10.1021/acsnano.3c11197
ACS Nano 2024, 18, 6359–6372

jumping; equilibrium shapes of the droplets with different volumes in contact with the MP; determination of the excess surface energy based on the areas of liquid−vapor and solid−liquid interfaces; determination of the critical volume below which the droplet is entrapped in the superhydrophobic groove; the pinch-off phenomenon observed in the experiment; influence of groove width on the MAJ behavior; influences of groove width and depth on the theoretical jumping height; influences of the MP size on the regime diagram for MAJ and the theoretical jumping height; influence of groove shape on the MAJ behavior; influence of surface hydrophilicity of the MPs on the MAJ behavior; schematic illustration showing the removal of MPs from the manipulated droplets after arriving at the destinations using electromagnetic fields; transportation of multiple droplets at the same time using MAJ; droplet jumping on chamfered SHGS; images showing the experimental setups for droplet climbing stairs and crossing obstacles (PDF)

Movie S1. Directional transportation of a droplet on the SHGS with circularly arrayed chamfered grooves using MAJ (MP4)

Movie S2. A droplet with an attached MP climbing the stairs based on MAJ (MP4)

Movie S3. A droplet with an attached MP crossing obstacles using MAJ (MP4)

Movie S4. Using MAJ to remotely add reactants for the microreaction (MP4)

AUTHOR INFORMATION

Corresponding Author

Shilin Huang − *School of Materials Science and Engineering, State Key Laboratory of Optoelectronic Materials and Technologies, Key Laboratory for Polymeric Composite and Functional Materials of Ministry of Education, Sun Yat-sen University, Guangzhou 510006, China*; Email: huangshlin@mail.sysu.edu.cn

Authors

Yusheng Huang − *School of Materials Science and Engineering, State Key Laboratory of Optoelectronic Materials and Technologies, Key Laboratory for Polymeric Composite and Functional Materials of Ministry of Education, Sun Yat-sen University, Guangzhou 510006, China*

Guifeng Wen − *School of Materials Science and Engineering, State Key Laboratory of Optoelectronic Materials and Technologies, Key Laboratory for Polymeric Composite and Functional Materials of Ministry of Education, Sun Yat-sen University, Guangzhou 510006, China*

Yue Fan − *School of Materials Science and Engineering, State Key Laboratory of Optoelectronic Materials and Technologies, Key Laboratory for Polymeric Composite and Functional Materials of Ministry of Education, Sun Yat-sen University, Guangzhou 510006, China*

Maomao He − *State Key Laboratory of Fine Chemicals, Frontiers Science Center for Smart Materials Oriented Chemical Engineering, Dalian University of Technology, Dalian 116024, China*

Wen Sun − *State Key Laboratory of Fine Chemicals, Frontiers Science Center for Smart Materials Oriented Chemical Engineering, Dalian University of Technology, Dalian 116024, China*; orcid.org/0000-0003-4316-5350

Xuelin Tian − *School of Materials Science and Engineering, State Key Laboratory of Optoelectronic Materials and Technologies, Key Laboratory for Polymeric Composite and Functional Materials of Ministry of Education, Sun Yat-sen University, Guangzhou 510006, China*; orcid.org/0000-0001-6178-2067

Complete contact information is available at: https://pubs.acs.org/10.1021/acsnano.3c11197

Author Contributions

The manuscript was written through contributions of all authors. All authors have given approval to the final version of the manuscript.

Notes

The authors declare no competing financial interest.

ACKNOWLEDGMENTS

The work was supported by National Natural Science Foundation of China (Nos. 12072381, 22072185, 21805315), Guangdong Basic and Applied Basic Research Foundation (No. 2019A1515012030), and Science and Technology Innovation Project of Guangzhou (202102020263). The authors acknowledge the National Supercomputer Center in Guangzhou for the use of the high-performance computing facility.

REFERENCES

(1) Chen, H.; Ran, T.; Gan, Y.; Zhou, J.; Zhang, Y.; Zhang, L.; Zhang, D.; Jiang, L. Ultrafast Water Harvesting and Transport in Hierarchical Microchannels. *Nat. Mater.* **2018**, *17*, 935−942.

(2) Bai, H.; Wang, X.; Li, Z.; Wen, H.; Yang, Y.; Li, M.; Cao, M. Improved Liquid Collection on a Dual-Asymmetric Superhydrophilic Origami. *Adv. Mater.* **2023**, *35*, No. 2209556.

(3) Gao, S.; Wang, Y.; Zhang, C.; Jiang, M.; Wang, S.; Wang, Z. Tailoring Interfaces for Atmospheric Water Harvesting: Fundamentals and Applications. *Matter.* **2023**, *6*, 2182−2205.

(4) Ghosh, R.; Baut, A.; Belleri, G.; Kappl, M.; Butt, H.; Schutzius, T. M. Photocatalytically Reactive Surfaces for Simultaneous Water Harvesting and Treatment. *Nat. Sustain.* **2023**, *6*, 1663−1672.

(5) Cho, H. J.; Preston, D. J.; Zhu, Y.; Wang, E. N. Nanoengineered Materials for Liquid-Vapour Phase-Change Heat Transfer. *Nat. Rev. Mater.* **2017**, *2*, 16092.

(6) Zhu, J.; Luo, Y.; Tian, J.; Li, J.; Gao, X. Clustered Ribbed-Nanoneedle Structured Copper Surfaces with High-Efficiency Dropwise Condensation Heat Transfer Performance. *ACS Appl. Mater. Interfaces.* **2015**, *7*, 10660−10665.

(7) Li, J.; Ha, N. S.; Liu, T. L.; van Dam, R. M.; 'CJ' Kim, C. Ionic-Surfactant-Mediated Electro-Dewetting for Digital Microfluidics. *Nature* **2019**, *572*, 507−510.

(8) Tian, T.; Shu, B.; Jiang, Y.; Ye, M.; Liu, L.; Guo, Z.; Han, Z.; Wang, Z.; Zhou, X. An Ultralocalized Cas13a Assay Enables Universal and Nucleic Acid Amplification-Free Single-Molecule RNA Diagnostics. *ACS Nano* **2021**, *15*, 1167−1178.

(9) Zeng, X.; Qian, L.; Yuan, X.; Zhou, C.; Li, Z.; Cheng, J.; Xu, S.; Wang, S.; Pi, P.; Wen, X. Inspired by Stenocara Beetles: From Water Collection to High-Efficiency Water-in-Oil Emulsion Separation. *ACS Nano* **2017**, *11*, 760−769.

(10) Tao, M.; Xue, L.; Liu, F.; Jiang, L. An Intelligent Superwetting PVDF Membrane Showing Switchable Transport Performance for Oil/Water Separation. *Adv. Mater.* **2014**, *26*, 2943−2948.

(11) Park, K. C.; Kim, P.; Grinthal, A.; He, N.; Fox, D.; Weaver, J. C.; Aizenberg, J. Condensation on Slippery Asymmetric Bumps. *Nature.* **2016**, *531*, 78−82.

(12) Huang, S.; Li, J.; Liu, L.; Zhou, L.; Tian, X. Lossless Fast Drop Self-Transport on Anisotropic Omniphobic Surfaces: Origin and Elimination of Microscopic Liquid Residue. *Adv. Mater.* **2019**, *31*, No. 1901417.
(13) Tang, X.; Huang, J.; Guo, Z.; Liu, W. A Combined Structural and Wettability Gradient Surface for Directional Droplet Transport and Efficient Fog Collection. *J. Colloid Interface Sci.* **2021**, *604*, 526–536.
(14) Zhang, L.; Guo, Z.; Sarma, J.; Zhao, W.; Dai, X. Gradient Quasi-Liquid Surface Enabled Self-Propulsion of Highly Wetting Liquids. *Adv. Funct. Mater.* **2021**, *31*, No. 2008614.
(15) Chen, K.; Zhu, J.; Tan, Y.; Sun, F.; Gan, J.; Peng, H.; Zhan, T.; Lyu, J. Development of Gradient-Wetting Janus Wood Membrane with High-Efficiency Fog Collection and Oil-Water Separation. *Chem. Eng. J.* **2023**, *470*, No. 144356.
(16) Yang, X.; Zhuang, K.; Lu, Y.; Wang, X. Creation of Topological Ultraslippery Surfaces for Droplet Motion Control. *ACS Nano* **2021**, *15*, 2589–2599.
(17) Huang, S.; Song, J.; Lu, Y.; Chen, F.; Zheng, H.; Yang, X.; Liu, X.; Sun, J.; Carmalt, C. J.; Parkin, I. P.; Xu, W. Underwater Spontaneous Pumpless Transportation of Nonpolar Organic Liquids on Extreme Wettability Patterns. *ACS Appl. Mater. Interfaces.* **2016**, *8*, 2942–2949.
(18) Yang, X.; Song, J.; Liu, J.; Liu, X.; Jin, Z. A Twice Electrochemical-Etching Method to Fabricate Superhydrophobic-Superhydrophilic Patterns for Biomimetic Fog Harvest. *Sci. Rep.* **2017**, *7*, 8816.
(19) Li, J.; Qin, Q. H.; Shah, A.; Ras, R. H. A.; Tian, X.; Jokinen, V. Oil Droplet Self-Transportation on Oleophobic Surfaces. *Sci. Adv.* **2016**, *2*, No. 1600148.
(20) Sun, Q.; Wang, D.; Li, Y.; Zhang, J.; Ye, S.; Cui, J.; Chen, L.; Wang, Z.; Butt, H. J.; Vollmer, D.; Deng, X. Surface Charge Printing for Programmed Droplet Transport. *Nat. Mater.* **2019**, *18*, 936–941.
(21) Wang, F.; Sun, Y.; Zong, G.; Liang, W.; Yang, B.; Guo, F.; Yangou, C.; Wang, Y.; Zhang, Z. Electrothermally Assisted Surface Charge Density Gradient Printing to Drive Droplet Transport. *ACS Appl. Mater. Interfaces.* **2022**, *14*, 3526–3535.
(22) Yin, K.; Wang, L.; Deng, Q.; Huang, Q.; Jiang, J.; Li, G.; He, J. Femtosecond Laser Thermal Accumulation-Triggered Micro-/Nano-structures with Patternable and Controllable Wettability Towards Liquid Manipulating. *Nano-Micro Lett.* **2022**, *14*, 97.
(23) Jin, Y.; Liu, X.; Xu, W.; Sun, P.; Huang, S.; Yang, S.; Yang, X.; Wang, Q.; Lam, R.; Li, R.; Wang, Z. Charge-Powered Electrotaxis for Versatile Droplet Manipulation. *ACS Nano* **2023**, *17*, 10713–10720.
(24) Sun, S.; Miao, J.; Tan, R.; Zhang, T.; Li, G.; Shen, Y. Asymmetric Soft-Structure Functional Surface for Intelligent Liquids' Distinction, Transportation, and Reaction Mixer. *Adv. Funct. Mater.* **2023**, *33*, No. 2209769.
(25) Wu, D.; Zhang, Z.; Zhang, Y.; Jiao, Y.; Jiang, S.; Wu, H.; Li, C.; Zhang, C.; Li, J.; Hu, Y.; Li, G.; Chu, J.; Jiang, L. High-Performance Unidirectional Manipulation of Microdroplets by Horizontal Vibration on Femtosecond Laser-Induced Slant Microwall Arrays. *Adv. Mater.* **2020**, *32*, No. 2005039.
(26) Zhang, Y.; Jiang, S.; Hu, Y.; Wu, T.; Zhang, Y.; Li, H.; Li, A.; Zhang, Y.; Wu, H.; Ding, Y.; Li, E.; Li, J.; Wu, D.; Song, Y.; Chu, J. Reconfigurable Magnetic Liquid Metal Robot for High-Performance Droplet Manipulation. *Nano Lett.* **2022**, *22*, 2923–2933.
(27) He, Y.; Yin, K.; Wang, L.; Wu, T.; Deng, Q.; Dou, Y.; Arnusch, C. J. Magnetically Actuated Superhydrophilic Robot Sphere Fabricated by a Femtosecond Laser for Droplet Steering. *Nano Lett.* **2023**, *23*, 4947–4955.
(28) Jing, X.; Chen, H.; Zhang, L.; Zhao, S.; Wang, Y.; Wang, Z.; Zhou, Y. Accurate Magneto-Driven Multi-Dimensional Droplet Manipulation. *Adv. Funct. Mater.* **2023**, *33*, No. 2210883.
(29) Dai, H.; Gao, C.; Sun, J.; Li, C.; Li, N.; Wu, L.; Dong, Z.; Jiang, L. Controllable High-Speed Electrostatic Manipulation of Water Droplets on a Superhydrophobic Surface. *Adv. Mater.* **2019**, *31*, No. 1905449.
(30) Chen, C.; Huang, Z.; Jiao, Y.; Shi, L.; Zhang, Y.; Li, J.; Li, C.; Lv, X.; Wu, S.; Hu, Y.; Zhu, W.; Wu, D.; Chu, J.; Jiang, L. *In Situ* Reversible Control Between Sliding and Pinning for Diverse Liquids under Ultra-Low Voltage. *ACS Nano* **2019**, *13*, 5742–5752.
(31) Kwon, G.; Panchanathan, D.; Mahmoudi, S. R.; Gondal, M. A.; McKinley, G. H.; Varanasi, K. K. Visible Light Guided Manipulation of Liquid Wettability on Photoresponsive Surfaces. *Nat. Commun.* **2017**, *8*, 14968.
(32) Wang, F.; Liu, M.; Liu, C.; Huang, C.; Zhang, L.; Cui, A.; Hu, Z.; Du, X. Light Control of Droplets on Photo-Induced Charged Surfaces. *Natl. Sci. Rev.* **2023**, *10*, No. nwac164.
(33) Yuan, Z.; Lu, C.; Liu, C.; Bai, X.; Zhao, L.; Feng, S.; Liu, Y. Ultrasonic Tweezer for Multifunctional Droplet Manipulation. *Sci. Adv.* **2023**, *9*, No. eadg2352.
(34) Li, J.; Kim, C. C. Current Commercialization Status of Electrowetting-on-Dielectric (EWOD) Digital Microfluidics. *Lab Chip.* **2020**, *20*, 1705–1712.
(35) Zhang, Y.; Nguyen, N. Magnetic Digital Microfluidics—a Review. *Lab Chip.* **2017**, *17*, 994–1008.
(36) Guo, R.; Ouyang, M.; Fan, Y.; Tian, X.; Huang, S. Capillary-Bridge Mediated Manipulation of Nonmagnetic Droplets Using Low Magnetic Fields with Self-Locking Feature. *Adv. Mater. Technol.* **2022**, *7*, No. 2200335.
(37) Lin, Y.; Hu, Z.; Zhang, M.; Xu, T.; Feng, S.; Jiang, L.; Zheng, Y. Magnetically Induced Low Adhesive Direction of Nano/Micropillar Arrays for Microdroplet Transport. *Adv. Funct. Mater.* **2018**, *28*, No. 1800163.
(38) Zhou, Y.; Huang, S.; Tian, X. Magnetoresponsive Surfaces for Manipulation of Nonmagnetic Liquids: Design and Applications. *Adv. Funct. Mater.* **2020**, *30*, No. 1906507.
(39) Shao, K.; Jiang, S.; Hu, Y.; Zhang, Y.; Li, C.; Zhang, Y.; Li, J.; Wu, D.; Chu, J. Bioinspired Lubricated Slippery Magnetic Responsive Microplate Array for High Performance Multi-Substance Transport. *Adv. Funct. Mater.* **2022**, *32*, No. 2205831.
(40) Foresti, D.; Poulikakos, D. Acoustophoretic Contactless Elevation, Orbital Transport and Spinning of Matter in Air. *Phys. Rev. Lett.* **2014**, *112*, 24301.
(41) Liu, C.; Liu, X.; Tang, Q.; Zhou, W.; Ma, Y.; Gong, Z.; Chen, J.; Zheng, H.; Joo, S. W. Three-Dimensional Droplet Manipulation with Electrostatic Levitation. *Anal. Chem.* **2022**, *94*, 8217–8225.
(42) Si, Y.; Hu, J.; Dong, Z. Bioinspired Magnetically Driven Liquid Manipulation as Microrobot. *Cell Rep. Phys. Sci.* **2021**, *2*, No. 100439.
(43) Mi, Y.; Liu, X.; Gao, Z.; Wang, M.; Shi, L.; Zhang, X.; Gao, K.; Mugisha, E. R.; Yan, W. 3D Photovoltaic Router of Water Microdroplets Aiming at Free-Space Microfluidic Transportation. *ACS Appl. Mater. Interfaces.* **2021**, *13*, 45018–45032.
(44) Li, N.; Wu, L.; Yu, C.; Dai, H.; Wang, T.; Dong, Z.; Jiang, L. Ballistic Jumping Drops on Superhydrophobic Surfaces *via* Electrostatic Manipulation. *Adv. Mater.* **2018**, *30*, No. 1703838.
(45) Boreyko, J. B.; Chen, C. Self-Propelled Dropwise Condensate on Superhydrophobic Surfaces. *Phys. Rev. Lett.* **2009**, *103*, No. 184501.
(46) Chen, X.; Patel, R. S.; Weibel, J. A.; Garimella, S. V. Coalescence-Induced Jumping of Multiple Condensate Droplets on Hierarchical Superhydrophobic Surfaces. *Sci. Rep.* **2016**, *6*, 18649.
(47) Zhang, K.; Li, Z.; Maxey, M.; Chen, S.; Karniadakis, G. E. Self-Cleaning of Hydrophobic Rough Surfaces by Coalescence-Induced Wetting Transition. *Langmuir.* **2019**, *35*, 2431–2442.
(48) Yan, X.; Qin, Y.; Chen, F.; Zhao, G.; Sett, S.; Hoque, M. J.; Rabbi, K. F.; Zhang, X.; Wang, Z.; Li, L.; Chen, F.; Feng, J.; Miljkovic, N. Laplace Pressure Driven Single-Droplet Jumping on Structured Surfaces. *ACS Nano* **2020**, *14*, 12796–12809.
(49) Chu, F.; Yan, X.; Miljkovic, N. How Superhydrophobic Grooves Drive Single-Droplet Jumping. *Langmuir.* **2022**, *38*, 4452–4460.
(50) Liu, Y.; Li, X.; Lu, C.; Yuan, Z.; Liu, C.; Zhang, J.; Zhao, L. High-Efficiency Directional Ejection of Coalesced Drops on a Circular Groove. *Langmuir.* **2022**, *38*, 4028–4035.

https://doi.org/10.1021/acsnano.3c11197
ACS Nano 2024, 18, 6359–6372

(51) Huh, C.; Mason, S. G. Effects of Surface Roughness on Wetting (Theoretical). *J. Colloid Interface Sci.* **1977**, *60*, 11−38.
(52) Schellenberger, F.; Encinas, N.; Vollmer, D.; Butt, H. J. How Water Advances on Superhydrophobic Surfaces. *Phys. Rev. Lett.* **2016**, *116*, 96101.
(53) de Gennes, P.-G.; Brochard-Wyart, F.; Quéré, D. *Capillarity and Wetting Phenomena: Drops, Bubbles, Pearls, Waves*; Springer: New York, 2004; pp 6−9.
(54) Wang, G.; Fei, L.; Luo, K. H. Lattice Boltzmann Simulation of Water Droplet Impacting a Hydrophobic Plate with a Cylindrical Pore. *Phys. Rev. Fluids.* **2020**, *5*, No. 083602.
(55) Papadopoulos, P.; Mammen, L.; Deng, X.; Vollmer, D.; Butt, H. J. How Superhydrophobicity Breaks Down. *Proc. Natl. Acad. Sci. U. S. A.* **2013**, *110*, 3254−3258.
(56) Brakke, K. A. The Surface Evolver. *Exp. Math.* **1992**, *1*, 141−165.
(57) Qian, B.; Loureiro, M.; Gagnon, D. A.; Tripathi, A.; Breuer, K. S. Micron-Scale Droplet Deposition on a Hydrophobic Surface Using a Retreating Syringe. *Phys. Rev. Lett.* **2009**, *102*, No. 164502.
(58) Feng, Y.; Zhao, W.; Duan, Y.; Zhu, S.; Zhang, X.; Thoraval, M. Attachment of a Particle to a Pendant Drop: How Large Can We Go? *Phys. Fluids* **2022**, *34*, No. 032120.
(59) Xia, Y.; Chen, H.; Li, J.; Hu, H.; Qian, Q.; He, R.; Ding, Z.; Guo, S. Acoustic Droplet-Assisted Superhydrophilic-Superhydrophobic Microarray Platform for High-Throughput Screening of Patient-Derived Tumor Spheroids. *ACS Appl. Mater. Interfaces.* **2021**, *13*, 23489−23501.
(60) Häcker, G. The Morphology of Apoptosis. *Cell Tissue Res.* **2000**, *301*, 5−17.
(61) Harvey, P. A.; Nguyen, A. V.; Evans, G. M. Influence of Electrical Double-Layer Interaction on Coal Flotation. *J. Colloid Interface Sci.* **2002**, *250*, 337−343.
(62) Kandow, C. E.; Georges, P. C.; Janmey, P. A.; Beningo, K. A. Polyacrylamide Hydrogels for Cell Mechanics: Steps Toward Optimization and Alternative Uses. *Methods Cell Biol.* **2007**, *83*, 29.

https://doi.org/10.1021/acsnano.3c11197
ACS Nano 2024, 18, 6359−6372